RSC Advances

PAPER

View Article Online
View Journal | View Issue

Cite this: *RSC Adv.*, 2024, **14**, 15791

Optimization of switching charge and recoverable energy density mediated by structural transformation in Sr-substituted $BaNiO_3$ perovskites

Rana Muhammad Ahmad Khan Manj,[a] Shahid M. Ramay,[b] M. A. Shar,[c] Shahzad Naseem[a] and Shahid Atiq *[a]

Because of their distinctive characteristics, ferroelectric perovskites are considered among the most potent and auspicious candidates for energy storage and pulsed power devices. But their energy storage properties and switching capabilities need to be further enhanced which can be done by substitutions of appropriate cations. Hence, a series of lead-free $Ba_{1-x}Sr_xNiO_3$ ($x = 0.00$, 0.33, 0.67, and 1.00) ceramics was fabricated using a sol–gel auto combustion technique. Rietveld's refinement of X-ray diffraction plots verified the complete development of the required hexagonal perovskite structure. Scanning electron microscopy images revealed a gradual increase in average grain sizes and agglomeration with the increase in Sr-content. Moreover, the existence of all the constituent elements exactly in proportion to their stoichiometric ratios was verified by energy dispersive X-ray spectroscopy. The characteristic parameters of ferroelectric materials such as ferroelectric response, electrical conductivity, and switching charge density were also determined. The *P*–*E* loops indicated that with the increase in Sr-content, the coercive field, remanent polarization, and maximum polarization all decreased gradually, but the recoverable energy density (W_{rec}) increased as the loops became slimmer. The maximum value of W_{rec} was found in the $Ba_{0.33}Sr_{0.67}NiO_3$ sample. Moreover, $SrNiO_3$ exhibited minimum energy loss with the highest efficiency of ~47.21%. The existence of a current barrier in all the samples was proved from the low leakage current values (~10^{-7} A). In addition, the pure $SrNiO_3$ showed a low electrical conductivity and minimum value of switching charge density. All these findings make $SrNiO_3$ a promising candidate for fast switching and energy storage applications.

Received 24th February 2024
Accepted 26th April 2024

DOI: 10.1039/d4ra01439a

rsc.li/rsc-advances

1. Introduction

With the exponential growth of the human population and rapid industrialization in the past few decades, environmental pollution and energy crises have become two major problems that humanity has ever faced.[1] Non-renewability of fossil fuels and the adverse environmental effects of their use have encouraged researchers to explore new renewable, cost-effective, and eco-friendly energy resources such as geothermal, wind, and solar energy, but the high intermittence of these resources has created a huge need for reliable and efficient energy storage equipment.[2–4] In comparison with batteries, electrochemical capacitors, and fuel cells, over time, dielectric capacitors have gained a lot of attention because of their ultrahigh power density, superior temperature stability, faster charging/discharging speeds, and longer service life. Thus, they are extensively used for pulsed power applications in hybrid electric vehicles, high-power weapon systems, particle accelerators, space technology, and power transmission systems.[5,6] Even though over 25% of the volume of pulsed power systems accounts for dielectric capacitors, these applications are severely impeded due to their lower energy storage density (W_T) and lower energy efficiency (η) of the dielectric materials that currently exist.[7–9] Hence, it is imperative to design and develop such dielectric materials that enhance the strength, energy storage properties and switching capabilities of dielectric capacitors.

Presently, ceramics and polymers are two key materials used for developing dielectrics. Polymer-based dielectrics generally exhibit large recoverable energy density (W_{rec}) and high dielectric breakdown strength (E_b), but low energy efficiency and temperature instability hold them back in many applications.[10,11] On the other hand, a higher dielectric constant, superior energy storage efficiency, better mechanical properties,

[a]*Centre of Excellence in Solid State Physics, University of the Punjab, Lahore-54590, Pakistan. E-mail: satiq.cssp@pu.edu.pk*

[b]*Department of Physics, College of Science, King Saud University (KSU), Riyadh, Saudi Arabia*

[c]*Department of Mechanical & Energy Systems Engineering, Faculty of Engineering and Informatics, University of Bradford, Bradford BD7 1DP, UK*

and exceptional temperature stability of ceramic-based dielectrics make them more suitable for use as dielectric capacitors.[12–14] Among the ceramic dielectrics, lead-based antiferroelectric and relaxor ferroelectric materials such as (Pb,La)(Zr,Ti)O_3 and (Pb,La)(Zr,Sn,Ti)O_3 have captured quite a bit of attention in the past decades, because of their high maximum polarization (P_{max}), low remanent polarization (P_r) and moderate E_b which led them to have large W_{rec} and high η.[15–18] However, considering the high toxicity of Pb and its adverse effects on the global environment and human health, researchers are now motivated to replace lead-based ceramics with new energy storage materials. Thus, lead-free ferroelectric ceramics have recently been proven to be eco-friendly energy storage materials.[19–23] Among them, those materials that have perovskite structures are regarded as highly promising candidates for energy storage and switching capabilities.[24]

Perovskite oxides have the general formula ABO_3, where mono, di, or tri-valent cations of alkali or alkaline earth metals occupy the A-sites whereas tetra, penta or hexavalent cations of transition metals occupy the B-sites.[25,26] A perfect crystalline unit cell of perovskite has cubic symmetry with a $pm\bar{3}m$ space group where each B-site cation is coordinated by six oxygen anions in a BO_3 octahedron framework, and each A-site cation reclined in the 12-fold coordinated site in between the octahedra.[27,28] The reason behind the ferroelectricity in these oxides is the creation of an electric dipole because of the displacement of the B-site cation from the centre of symmetry in the 001, 110 or 111 directions, leading towards the tetragonal, orthorhombic, or rhombohedral structures, respectively, under the Curie temperature.[29] Exceptional structural stability under the prospect of adaptation of different compositions by changing different cations, either on the A-site or on the B-site, is the key reason for the characteristic excellence of these materials.[30] Several ferroelectric perovskites such as $BaSnO_3$, (Na,Bi)TiO_3, Ba(Zr,Ti)O_3 and (Ba,Sr)TiO_3 have been reported to have good energy storage characteristics.[1,18,22,25]

Recently, many researchers have been studying the energy storage capabilities of the ferroelectric perovskites. For example, Zhang *et al.* investigated the improved energy density and higher efficiency in $Bi_{0.5}Na_{0.5}TiO_3$ (BNT) under a low electric field.[31] Furthermore, Yu *et al.* studied the $BaZrO_3$ substituted BNT-based ceramic where the Ba^{2+} substitution on the Na^+ site caused a decrease in grain size and P_r, while enhancing the breakdown strength together with the higher temperature stability.[18] In another paper, Huang *et al.* reported a nearly linear *P–E* behavior in $Ba_{0.4}Sr_{0.6}TiO_3$ ceramic fabricated by a cost-effective sol–gel route which resulted in an enhanced E_b and W_{rec} together with an ultrahigh efficiency.[32] Similarly, Khalil and Wahba addressed the enhancements in structural stability and dielectric properties in Sr-substituted $LaNiO_3$.[33] Moreover, Hasan *et al.* used a theoretical approach to describe the structural stability and electronic behavior in $SrNiO_3$.[34] But apart from these, switching charge density is also one of the key figures of merit for dielectric materials. Hence, Mahmoud and Parashar investigated the decrease in leakage current and switching charge density in $(Ba_{1-x}Ca_x)TiO_3$ ceramic using a positive-up-negative-down (PUND) analysis.[35] Thus, these contemporary efforts have motivated us to investigate the tunability in structural and morphological properties, ferroelectric behavior, and fast switching capabilities in Sr-substituted $BaNiO_3$ which is the main focus of this work.

2. Experimental

2.1. Sample synthesis

A sol–gel auto combustion route was employed for the fabrication of eco-friendly $Ba_{1-x}Sr_xNiO_3$ ($x = 0.00$, 0.33, 0.67, and 1.00) ceramics. In the preparation, metal nitrates such as $Sr(NO_3)_2$ (≥98.0%), $Ba(NO_3)_2$ (≥98.0%) and $Ni(NO_3)_2 \cdot 6H_2O$ (≥98.0%), were procured from Sigma-Aldrich, utilized as precursors, whereas glycine [NH_2CH_2COOH] and urea [$CO(NH_2)_2$] of analytical grade, were purchased from Riedel-de Haën and Honeywell, respectively, and were used as the fuel. After stoichiometric calculations, the aqueous solutions of each material were prepared separately by dissolving the estimated quantities in deionized water, and the metal-to-fuel ratios were kept at 2 : 3. Furthermore, these separate solutions were fused in a larger beaker and a magnetic stirrer was placed in it. Then, the beaker was put on a hot plate at a temperature of 90 °C and left stirring at 250 rpm. After approximately 2 h, it was observed that a thick solution (gel) had been formed which impeded the motion of the magnetic stirrer. At that moment, the stirrer was removed from the beaker and the temperature was raised gradually up to 190 °C for the removal of moisture and residual gasses which turned the gel into a thick paste. Next, the temperature was steadily increased further, and at 270 °C a vigorous exothermic reaction took place which turned the paste into an ash-like dark and fluffy powder. After cooling, these ashes were converted into a homogeneous powder by grinding in agate mortar and pestle. Then, for the development of the proper phase, the fine powder was calcined in a box furnace at 850 °C for 3 h. Finally, pellets of approximately 1 mm thickness and 7 mm diameter were made from the calcined powder by exerting a 30 kN compressive force in a Apex hydraulic press (Specac, UK). A schematic demonstration of the complete fabrication process is shown in Fig. 1.

2.2. Characterization

Structural analysis of all the fabricated samples was accomplished using a D8 ADVANCE X-ray diffractometer (Bruker). A Nova NanoSEM 450 (FEI) was employed for morphological examination by field emission scanning electron microscopy (FESEM). To confirm the elemental configuration energy dispersive X-ray spectroscopy (EDX) was used. The ferroelectric study of samples was conducted using a precision multiferroic analyzer (Radiant-Technologies Inc., Albuquerque, NM, USA).

3. Results and discussion

3.1. Phase and structural studies

Fig. 2(a) shows the X-ray diffraction (XRD) patterns of $Ba_{1-x}Sr_xNiO_3$ ($x = 0.00$, 0.33, 0.67, and 1.00) ceramic samples where the intensity peaks were obtained by applying CuK_α radiation (λ

Fig. 1 Schematic profile of sample preparation.

= 1.5406 Å) and the peaks were plotted against 2θ values ranging from 15° to 75°. Indexing of these patterns was done by the analytical procedure described by Cullity.[36] The XRD peaks for the pure $BaNiO_3$ (BN) sample at 2θ values of 18.32°, 26.02°, 31.78°, 37.78°, 41.48°, 49.78°, 53.22°, 56.74°, 60.78°, 63.58°, 66.52°, 70.24°, 72.56° were indexed as (100), (101), (110), (002), (201), (112), (211), (300), (103), (212), (220), (203), (311), respectively, and for the pure $SrNiO_3$ (SN) sample, the peaks at 2θ values of 19.10°, 26.54°, 33.36°, 36.98°, 41.82°, 43.20°, 54.56°, 55.78°, 59.76°, 65.62°, 70.28° were indexed as (100), (101), (110), (002), (102), (201), (202), (211), (300), (212), (220), respectively.

For all the peaks of the BN and SN samples, *hkl* values were perfectly matched with the ICSD cards #00-029-0196 and 00-025-0904, respectively, which confirmed that the pure phase hexagonal perovskite structure with a space group of $P6_3/mmc$ had a space group of # 194 for both the crystals as shown in Fig. 2(c). A similar hexagonal perovskite structure was seen in both the intermediate compositions (BSN-1 and BSN-2 for x = 0.33 and 0.67, respectively). However, some low-intensity diffraction peaks, represented by the club symbol (♣), also appeared in the intermediate compositions which indicated a minimal secondary phase of SrO that is also detected in other such materials.[37] In Fig. 2(b), a fine scan of the XRD patterns in the range from 23° to 30° of 2θ values shows that the (101) peak shifts towards the larger angle as the Sr-contents increase. This shift predicts the decrease in lattice parameters as of the inverse relationship between the lattice constants and the diffraction angle (2θ).[36]

The XRD patterns of the $Ba_{1-x}Sr_xNiO_3$ samples were further analyzed using Rietveld's refinement to obtain precise and quantitative phase analysis. The refinement was conducted using the X'pert HighScore Plus program using crystallographic

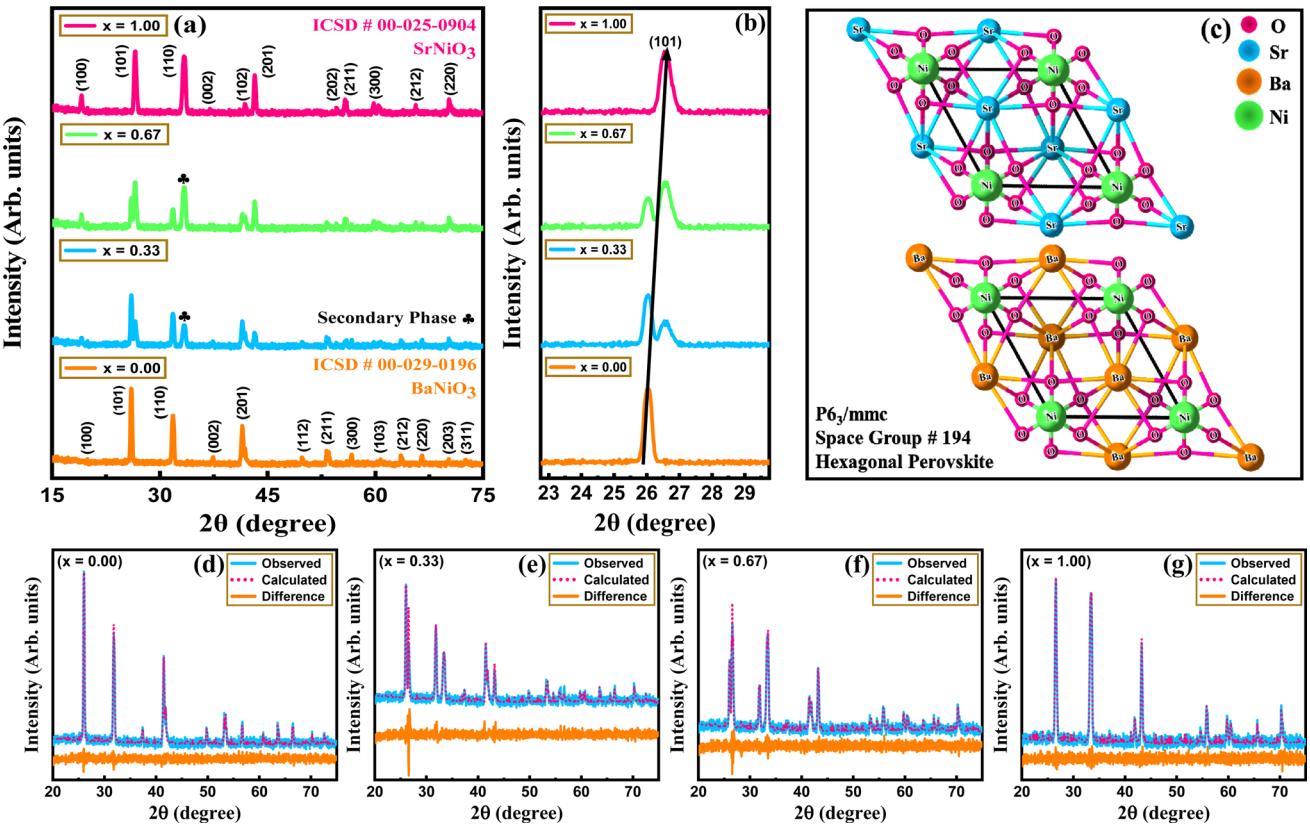

Fig. 2 (a) Indexed XRD patterns of the $Ba_{1-x}Sr_xNiO_3$ samples with x = 0.00, 0.33, 0.67, and 1.00, (b) shifting of the (101) peak towards higher angles, (c) crystal structure of $BaNiO_3$ and $SrNiO_3$, and (d)–(g) Rietveld's refined XRD patterns of the $Ba_{1-x}Sr_xNiO_3$ samples with x = 0.00, 0.33, 0.67, and 1.00.

information files (CIF) and the resulting patterns are shown in Fig. 2(d)–(g). It was noticed that all the observed and calculated XRD patterns were well matched and no considerable distortion has been seen in any pattern. The difference plots of the calculated and observed patterns are also shown by the orange lines in Fig. 2(d)–(g), where the minute difference in the intensities might be because of minor defects such as oxygen vacancies in the samples. Moreover, as stated earlier, a minimal secondary phase can also be observed from the peaks at the 2θ value of 33.36° in the difference plots of the BSN-1 and BSN-2 samples. In addition, to check the structural reliability, different structural refined parameters (R-factors), specifically, weighted profile (R_{wp}), expected weighted profile (R_{exp}), and profile (R_p) were also calculated using the following relationships:

$$R_{wp} = \left[\frac{\sum_i w_i (I_{ic} - I_{io})^2}{\sum_i w_i (I_{io})^2}\right]^{1/2} \quad (1)$$

$$R_{exp} = \left[\frac{N - P}{\sum_i w_i (I_{io})^2}\right]^{1/2} \quad (2)$$

$$R_p = \frac{\sum_i |I_{io} - I_{ic}|}{\sum_i |I_{io}|} \quad (3)$$

where w_i is the weight factor, I_{io} and I_{ic} represent the observed and calculated intensities at ith point of the diffraction profile, respectively, N is the number of experimentally observed points and P shows the fitting parameters.[38] From the values of R_{wp} and R_{exp}, the goodness of fit (χ^2) parameter was calculated using eqn (4):[39]

$$\chi^2 = \frac{R_{wp}}{R_{exp}} \quad (4)$$

Table 1 gives the calculated values of R_{exp}, R_{wp}, R_p and χ^2 for all the samples, where the low values of χ^2 are evidence of the development of the requisite crystalline phase in all the samples.

Moreover, from the XRD data, lattice constants 'a' and 'c', were calculated for all the samples. For the pure BN sample, the values were found to be 5.6247 Å and 4.8203 Å, respectively. With the increase in the substitution contents, lattice constant 'a' decreased in the intermediate samples, BSN-1 and BSN-2, but the value of c only increased slightly. For the pure SN sample, these values were found as 5.3541 Å and 4.8563 Å, respectively, as shown in Fig. 3(a). Overall, the volumes of the unit cells decreased as the Sr-content improved which is credited to the smaller radii of Sr^{2+} (1.44 Å) than that of Ba^{2+} (1.61 Å).[40]

Furthermore, the X-ray density (ρ_x), was calculated from the unit cell volume of each sample using eqn (5):

$$\rho_x = \frac{NM}{N_A V} \quad (5)$$

where M is the molar mass of the molecule, N represents the formula units per unit cell, V denotes the unit cell volume and N_A is Avogadro's number. Moreover, in all the prepared materials, bulk density (ρ_B) was evaluated by eqn (6):

$$\rho_B = \frac{m}{v} \quad (6)$$

where v ($v = \pi r^2 h$) and m denote the pellets' volume and mass, respectively.[41] Plots of these X-rays and bulk densities against

Table 1 Data obtained from Rietveld's refinement of the $Ba_{1-x}Sr_xNiO_3$ samples

$Ba_{1-x}Sr_xNiO_3$ (x)	R_{exp}	R_p	R_{wp}	χ^2
0.00	1.89	8.77	11.50	6.06
0.33	1.80	9.78	13.10	7.26
0.67	1.74	9.45	12.38	7.11
1.00	1.71	9.69	12.83	7.50

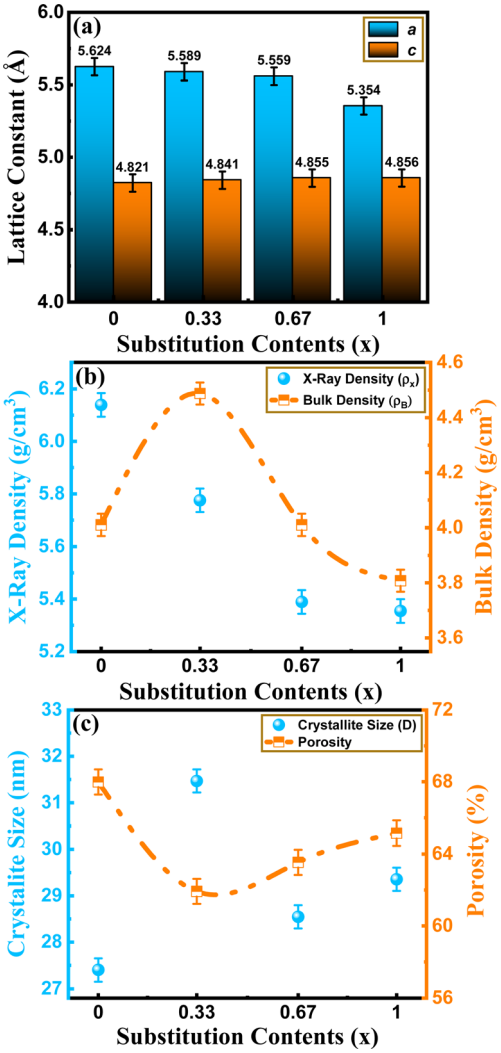

Fig. 3 Variation in (a) lattice constants, (b) X-ray and bulk densities, and (c) crystallite size and porosity with the increase in substitution contents.

the substitution contents are shown in Fig. 3(b). These plots show a decrease in X-ray density with the increase in Sr-content which is due to the relatively higher decrease in the molecular weight of the SN sample than that of the drop in its unit cell volume. From the values of the bulk and X-ray densities, the porosity of each sample was calculated using eqn (7):

$$\text{Porosity} = \left(1 - \frac{\rho_B}{\rho_x}\right) \times 100\% \quad (7)$$

Using the Debye–Scherrer relation, stated in eqn (8), the average crystallite size of the nanoparticles was evaluated for all the samples:

$$D = \frac{k\lambda}{\beta \cos\theta} \quad (8)$$

here θ denotes the Bragg's angle, β is the peak broadening or full-width at half-maxima (FWHM), k represents Scherrer's constant (shape factor), and λ is the wavelength of the X-rays (1.5406 Å for CuK_α).[42] It was observed that with the increase in substitution contents, the crystallite size increased, but the porosity first decreased for the BSN-1 sample and then gradually increased from 22.3% to 28.9%, however, it remained less than that of the pure BN sample (34.7%) as shown in Fig. 3(c).

The minor crystal distortions and imperfections may produce strain (ε) in the crystal lattice which causes peak broadening. Thus, for a better estimation of crystalline size, the Williamson–Hall (W–H) method was also employed using eqn (9):

$$\beta \cos\theta = \varepsilon(4 \sin\theta) + \frac{k\lambda}{D} \quad (9)$$

where β is FWHM, θ denotes the peak positions and ε represents the strain.[43] For all the samples, the plots were drawn between $\beta \cos\theta$ and $4 \sin\theta$ values using linear fitting and are shown in Fig. 4 where the slope of the line provides the value of induced strain while the crystallite size can be calculated from the y-intercept ($k\lambda/D$) for each sample. It can be seen that all the plots are showing negative slopes which clearly indicate the presence of compressive lattice strain in all the samples. However, the strain is minimum in the pure SN sample ($x = 1.00$) which indicates the strength of the material when compared to others. The calculated values of the structural parameters of all the prepared materials are listed in Table 2 where it can be observed that the crystallite sizes which were calculated by the W–H method were less than those calculated by Scherrer's formula which is due to the contribution of the strain values.[44]

3.2. Surface morphology

Fig. 5(a)–(d) show the FESEM images of the $Ba_{1-x}Sr_xNiO_3$ samples ($x = 0.00$, 0.33, 0.67, and 1.00) together with the particle size distribution histograms in the insets. All these images were captured by applying an external potential of 10 kV and have a magnification of 200 000×. For the measurement of the particle sizes, Java-based software 'ImageJ' was used. As can be seen in Fig. 5(a), for the pure BN sample, semi-spherical shaped grains with sharp boundaries having particle sizes in the 10 nm to 45 nm range were almost evenly distributed all over the surface of the material. However, by increasing the substitution contents, the grain sizes were slightly increased as can be observed in Fig. 5(b), for the BSN-1 sample, where the particle sizes are in the range of 15 nm to 45 nm. Moreover, the uniformity in the grain distribution was disturbed when an

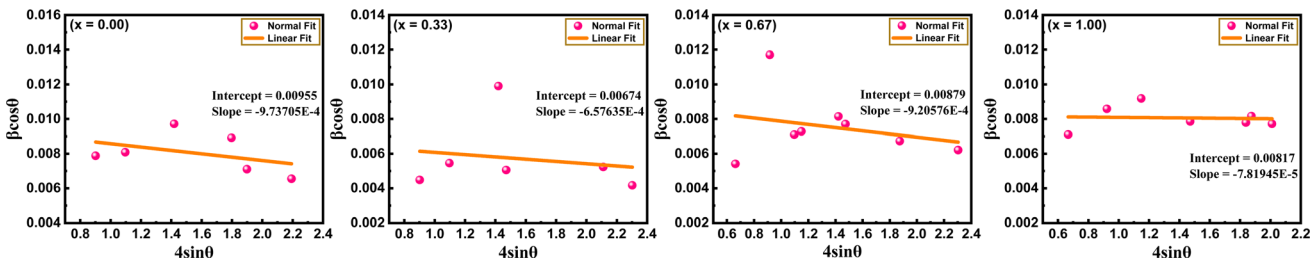

Fig. 4 Williamson–Hall plots of $Ba_{1-x}Sr_xNiO_3$ samples with $x = 0.00$, 0.33, 0.67, and 1.00.

Table 2 The calculated values of the lattice constants, unit cell volume, X-ray density, bulk density, porosity, and crystallite size obtained by Scherrer's formula and the Williamson–Hall plot method, and the strain of the $Ba_{1-x}Sr_xNiO_3$ samples

$Ba_{1-x}Sr_xNiO_3$		$x = 0.00$	$x = 0.33$	$x = 0.67$	$x = 1.00$
Lattice constants (Å) ± 0.06	a	5.6247	5.5892	5.5592	5.3541
	c	4.8203	4.8402	4.8557	4.8563
Unit cell volume (Å^3) ± 4.50		132.06	130.94	129.90	120.56
X-ray density (g cm^{-3}) ± 0.045		6.14	5.78	5.39	5.35
Bulk density (g cm^{-3}) ± 0.04		4.01	4.49	4.01	3.81
Porosity (%) ± 0.7		34.7	22.3	25.6	28.9
Crystallite size (nm) ± 0.25	Scherrer	27.40	31.46	28.54	29.35
	W–H	14.51	20.56	15.76	16.96
Strain (ε)		-9.74×10^{-4}	-6.58×10^{-4}	-9.21×10^{-4}	-7.82×10^{-5}

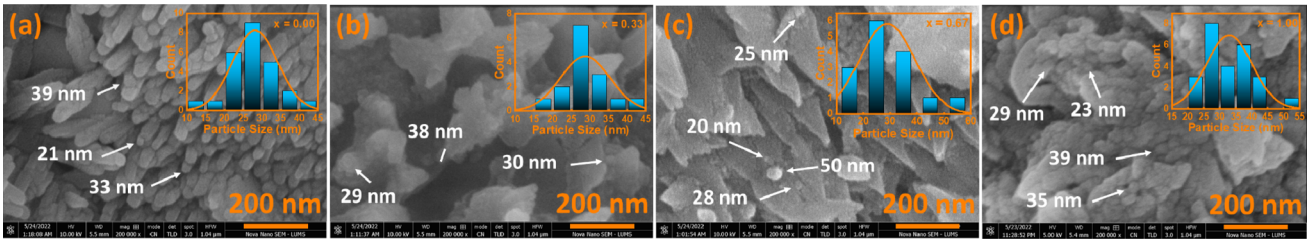

Fig. 5 SEM images of the $Ba_{1-x}Sr_xNiO_3$ samples with x = (a) 0.00, (b) 0.33, (c) 0.67, and (d) 1.00 captured at a magnification of 200 000×. The relevant in-sets show respective grain size distributions.

increase in agglomeration was noticed. For BSN-2 sample, particle sizes are in the 10 nm to 60 nm range as shown in Fig. 5(c). The reason for this increase is that SrO (2531 °C) has a higher melting point than that of BaO (1923 °C), so, with the increase in Sr-content, the $Ba_{1-x}Sr_xNiO_3$ samples have less of a liquid phase during heat treatment. Thus, the competition between the adjacent particles decreases and the probability of the precipitation of a new nucleus reduces, which results in the acceleration of the grain growth.[45] In both intermediate compositions *i.e.*, $x = 0.33$ and 0.67, voids and gaps can be seen between agglomerated grains which indicate a considerable increase in porosity. Finally, for the pure SN sample, particle sizes are in the 20 nm to 55 nm range as shown in Fig. 5(d), where a high agglomeration can also be observed which is due to the infusion of irregular spherical shaped grains during the heat treatment.[46]

3.3. Elemental analysis

Fig. 6 displays the EDX spectra of the prepared samples, which verified the existence of Ba, Ni, O, and Sr according to the exact stoichiometric ratios in the $Ba_{1-x}Sr_xNiO_3$ samples of different compositions. In all the spectra, peaks appearing at 0 keV of energy represent the reference peaks. It can be seen that in the pure BN sample, no Sr-peak was observed, which established the development of the pure phase of $BaNiO_3$. However, with the increase in the substitution contents, the Sr-peaks can be spotted together with the Ba, Ni, and O peaks in the BSN-1 and BSN-2 samples. Finally, in the pure SN sample, no Ba peak was detected, which proved the formation of pure $SrNiO_3$ by the complete substitution of Sr at the Ba site. Moreover, in all the samples, the existence of carbon (C) peaks is due to the adhesive tape that grasps the material on the sample holder.[47] In addition, the existence of gold (Au) peaks refers to the gold coating on the sample surface which is used for better conduction of the electronic beam.[41] Table 3 provides the exact weight percentages (wt%) of all the constituent elements in all the samples. It was observed that the wt% of Sr increased by increasing the substitution contents, and its maximum value is found in the pure SN sample. On the other hand, the wt% for Ba decreased with the increase in Sr-content, and this verifies the findings of EDX spectra.

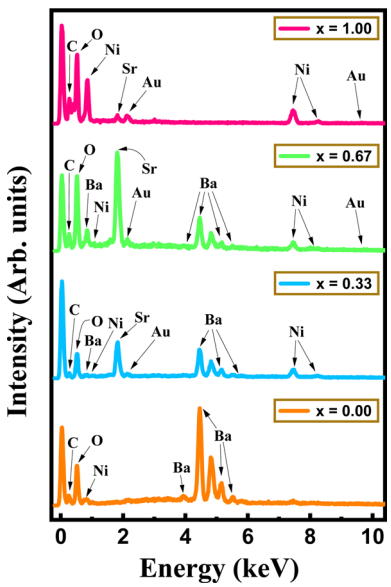

Fig. 6 EDX spectra of $Ba_{1-x}Sr_xNiO_3$ samples with $x = 0.00$, 0.33, 0.67, and 1.00.

3.4. Ferroelectric study

The characteristic ability of certain dielectric materials to reverse the spontaneous polarization (P) by an external electric field is known as ferroelectricity. This behavior is observed due to the orientation of the domains in the materials on applying the external field.[19] Being a prime characteristic of energy storage materials, ferroelectricity has completely modernized the electronic industry in the recent past. To determine the ferroelectric characteristics of the prepared $Ba_{1-x}Sr_xNiO_3$ samples, the *P–E* (polarization *versus* electric field) loops for all the different compositions ($x = 0.00$, 0.33, 0.67, and 1.00) were recorded at room temperature and the results are shown in Fig. 7(a). All these *P–E* hysteresis loops were obtained at an optimized test frequency of 1 kHz, under an applied 'ac' electric field of 150 V cm^{-1}. In all the samples, the uniform distribution of the electric dipoles was evident from the *P–E* loops' symmetry

Table 3 Elemental weight percentage in $Ba_{1-x}Sr_xNiO_3$ samples

	Weight percentage (%)					
$Ba_{1-x}Sr_xNiO_3$ (x)	C	O	Ni	Ba	Sr	Au
0.00	3.04	17.96	22.34	54.57	—	2.07
0.33	4.33	19.48	24.18	38.82	11.10	2.07
0.67	5.94	20.61	25.69	19.34	25.69	2.71
1.00	6.84	21.46	26.96	—	41.85	2.87

about the origin. Moreover, the trend of continuous enhancement of polarization as the strength of the electric field increased, demonstrated the linear ferroelectric behavior of the synthesized materials.[48] This dielectric response is due to the contribution of electronic, ionic, and dipolar polarizations in the material.[49] Apart from this, a leaky behavior was also observed from the *P–E* loops, which is due to the impact of the oxygen vacancies produced in samples during the initial sol–gel process. Most of these vacancies were equilibrated by atmospheric oxygen during calcination but some of them still remained behind which caused a leakage of current on application of the electric field.[50] Overall, this leakage behavior was reduced with the increase in the substituted contents and was found to be minimal in the pure SN sample. The charge–discharge curves for all the samples are shown in Fig. 7(b), where it can be observed that the area under the curves decreased continuously with the increase in the substitution contents which predicted minimum energy loss in the pure SN sample. Moreover, the discharging part of the curves shows that some domains still maintain the polarized state even after the removal of the external electric field.[51]

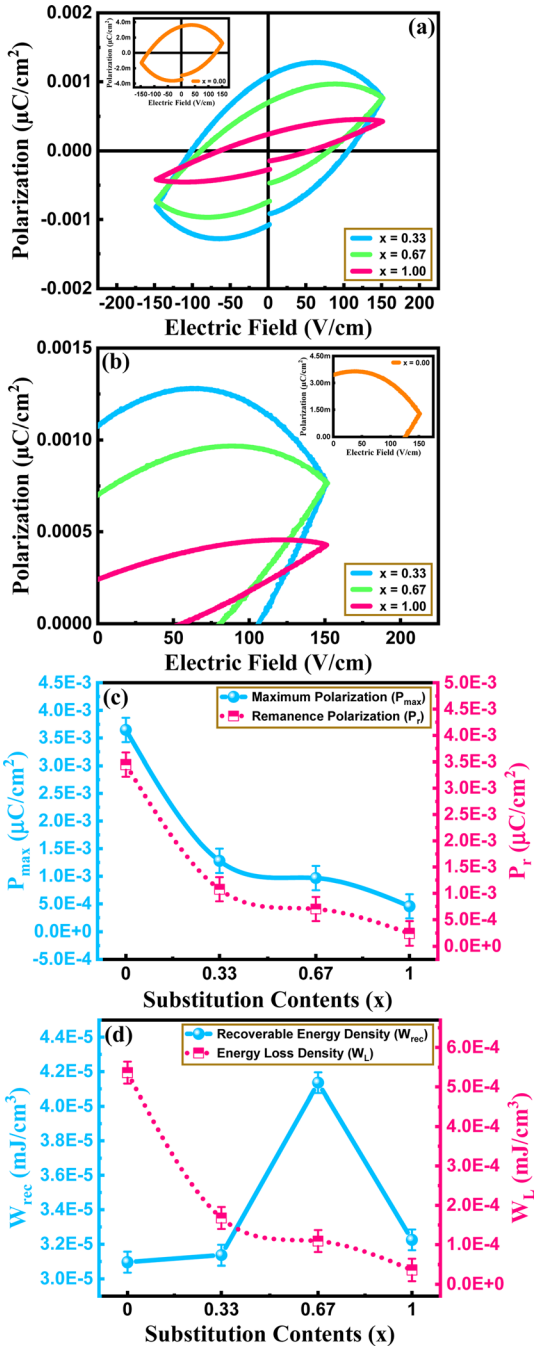

Fig. 7 (a) Polarization *versus* electric field hysteresis loops, (b) charge–discharge regions of the *P–E* loops, (c) variation in maximum and remanent polarization by changing the substitution content, and (d) change in recoverable energy density and energy loss density with increases in Sr-content in the $Ba_{1-x}Sr_xNiO_3$ samples with $x = 0.00$, 0.33, 0.67, and 1.00.

P–E loops were also used to find the exact values of the coercive field (E_c), maximum polarization (P_{max}), and remanent polarization (P_r) in all samples. Fig. 7(c) shows the plot of P_{max} and P_r against the substitution contents. It can be seen that P_{max} and P_r both decreased with the increase in the Sr-content which was due to the lower electric dipole polarizability of Sr (27.6×10^{-24} cm^3) than that of Ba (39.7×10^{-24} cm^3).[52] Table 4 gives the exact numbers of P_{max}, P_r, and E_c in all different samples where they vary from 3.65×10^{-3} to 0.45×10^{-3} μC cm^{-2}, from 3.45×10^{-3} to 0.24×10^{-3} μC cm^{-2} and from 122.74 to 61.92 V cm^{-1} respectively, with the increasing substitution contents. The *P–E* loops also served other purposes because the area confined between the discharge curve and the axis of polarization provides the recoverable energy density (W_{rec}). Similarly, the area of the loop gives the value of the energy loss density (W_L).[53] Using the values of P_{max} and P_r, the total and recoverable energy densities were calculated using the following equations:

$$W_T = \int_0^{P_{max}} E dP \quad (10)$$

$$W_{rec} = -\int_{P_r}^{P_{max}} E dP \quad (11)$$

where E represents the external electric field, and $dP = P_{max} - P_r$. From the values of W_{rec} and W_T, the energy loss density was calculated using eqn (12):[54]

$$W_L = W_T - W_{rec} \quad (12)$$

Fig. 7(d) shows the plot of W_{rec} and W_L against the substitution contents where an increase in W_{rec} can be noticed with the increase in the substituted content. The highest value of W_{rec} was obtained for the BSN-2 sample. However, a further increase in Sr-content caused a decrease in W_{rec} for the pure SN sample but the value is still greater than that of the pure BN sample. The W_L, on the other hand, decreased continuously with an increase in Sr-content, and the lowest value was found for the pure SN sample. From W_{rec} and W_L, the energy storage efficiency (η) was calculated for all the samples using eqn (13):[55]

$$\eta = \frac{W_{rec}}{W_{rec} - W_L} \times 100\% \quad (13)$$

Table 4 Maximum polarization (P_{max}), remanent polarization (P_r), and coercive field (E_c) in all the $Ba_{1-x}Sr_xNiO_3$ samples

$Ba_{1-x}Sr_xNiO_3$ (x)	P_{max} 10^{-3} (μC cm^{-2})	P_r 10^{-3} (μC cm^{-2})	E_c (V cm^{-1})
0.00	3.650	3.450	122.74
0.33	1.280	1.080	100.72
0.67	0.967	0.701	88.21
1.00	0.455	0.240	61.92

It can be seen from Fig. 8(a) that with the increase in substitution contents, the efficiency also increased and it was highest, at 47.21%, in the pure SN sample. Table 5 gives the exact calculated values of W_T, W_{rec}, and W_L in all the samples which vary from 0.068 × 10^{-3} to 0.567 × 10^{-3} mJ cm^{-3}, from 0.0310 × 10^{-3} to 0.0414 × 10^{-3} mJ cm^{-3} and from 0.036 × 10^{-3} to 0.536 × 10^{-3} mJ cm^{-3}, respectively.

For all the samples, the *P–E* loops were unsaturated under the applied electric field which is because of the fact that polarization is likely to be enhanced by strengthening the field.

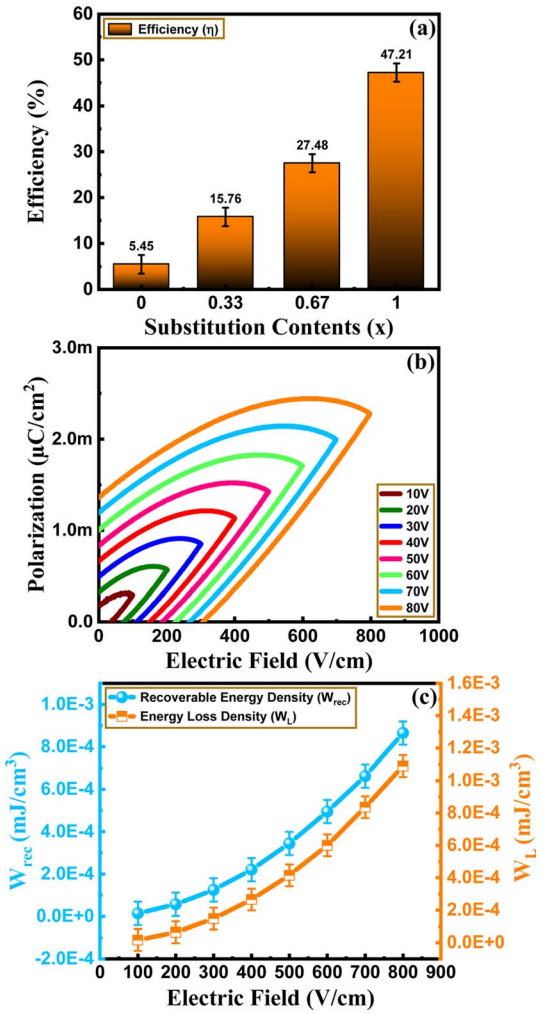

Fig. 8 (a) Percentage efficiency in all the $Ba_{1-x}Sr_xNiO_3$ samples, (b) charge–discharge curves, and (c) variation in recoverable energy density and energy loss density at different potentials in the pure $SrNiO_3$ sample.

Because the pure SN sample shows the best ferroelectric response, its *P–E* loops were further investigated at higher field strengths from over the range 100 V cm^{-1} to 800 V cm^{-1} as shown in Fig. 8(b). It was observed that the maximum polarization increased continuously with the increase in field strength which indicated that at higher field strengths, the dipole alignment has been improved. Fig. 8(c) exhibits a similar increasing trend for both W_{rec} and W_L when the electric field is strengthened. The exact values of P_{max}, P_r, E_c, W_T, W_{rec}, and W_L at different values of the electric field are listed in Table 6.

3.5. *I–V* characteristics

The Fowler–Nordheim tunnelling, grain-boundary conductivity, hooping conductivity, ohmic current, space charge limited current (SCLC), Poole–Frenkel emission, and Schottky emission are the major leakage pathways in ferroelectric materials.[56] Fig. 9(a) represents the *I–V* (leakage current *versus* voltage) curves for all the synthesized samples where the applied voltage was kept in the range of ±10 V. It was observed that in all the samples, the leakage current increased with an increase in applied voltage and showed a symmetrical behavior for the positive and negative voltages. Moreover, the values of the leakage current in the BSN-1 and BSN-2 samples (10^{-6} A), are higher than those of the pure BN and SN samples (10^{-7} A) which is due to the oxygen vacancies and the minor secondary phase in the intermediate compositions. Using the data obtained from the *I–V* measurements, the conductivity was calculated for all the samples and plotted against the substitution contents as shown in Fig. 9(b), where a trend similar to that of the *I–V* curves is repeated. Both the pure BN and pure SN samples showed lower conductivities, *i.e.*, 1.165 × 10^{-8} Ω^{-1} cm^{-1} and 1.20 × 10^{-8} Ω^{-1} cm^{-1}, respectively, which corresponds to their good ferroelectric response and shows the prospects of the material for practical applications in ultra-sensitive pulsating devices.

3.6. PUND analysis

Because the *P–E* loops' measurements are insufficient to distinguish between the contributions of domain switching and leakage current to the remanent polarization, to measure the accurate values of the remanent polarization (switching charge density), the positive-up-negative-down (PUND) technique was employed. This approach was first published by Scott *et al.* in 1989.[57] In their method, four identical voltage pulses are applied to the sample after initially setting it in the polarization state. The initial pulse is applied for the measurement of the total switching polarization (P*) which provides the combined

Table 5 Total stored energy density (W_T), recoverable energy density (W_{rec}), and energy loss density (W_L) in all the $Ba_{1-x}Sr_xNiO_3$ samples

$Ba_{1-x}Sr_xNiO_3$ (x)	W_T 10^{-3} (mJ cm^{-3})	W_{rec} 10^{-3} (mJ cm^{-3})	W_L 10^{-3} (mJ cm^{-3})
0.00	0.567	0.0310	0.536
0.33	0.199	0.0314	0.168
0.67	0.150	0.0414	0.109
1.00	0.068	0.0322	0.036

Table 6 Maximum polarization (P_{max}), remanent polarization (P_r), coercive field (E_c), total stored energy density (W_T), recoverable energy density, and energy loss density at different field strengths in the pure $SrNiO_3$ sample

Field strength (V cm^{-1})	P_{max} 10^{-3} (μC cm^{-2})	P_r 10^{-3} (μC cm^{-2})	E_c (V cm^{-1})	W_T 10^{-3} (mJ cm^{-3})	W_{rec} 10^{-3} (mJ cm^{-3})	W_L 10^{-3} (mJ cm^{-3})
100	0.308	0.168	−44.75	0.030	0.014	0.016
200	0.605	0.321	−86.42	0.121	0.056	0.064
300	0.910	0.494	−129.47	0.273	0.124	0.148
400	1.214	0.663	−174.54	0.485	0.220	0.265
500	1.519	0.830	−217.83	0.759	0.344	0.415
600	1.826	1.000	−264.37	1.095	0.495	0.600
700	2.141	1.194	−313.97	1.498	0.662	0.836
800	2.443	1.362	−359.46	1.954	0.864	1.089

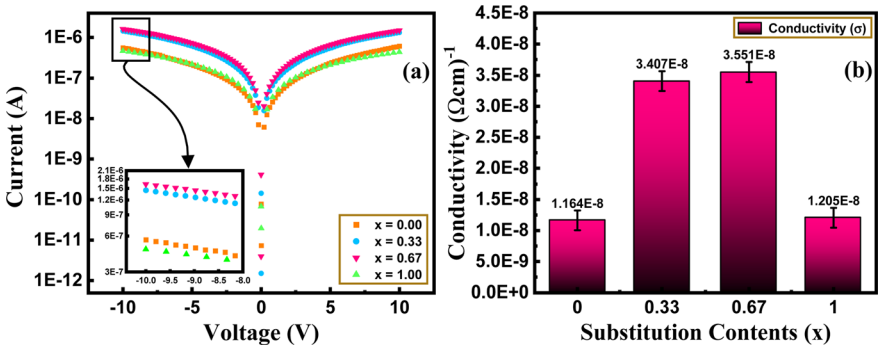

Fig. 9 (a) I–V characteristics curves and (b) the conductivity of the $Ba_{1-x}Sr_xNiO_3$ samples with x = 0.00, 0.33, 0.67, and 1.00.

effect of domain switching polarization and leakage current as shown by eqn (14):

$$P^* = P_{Switching} + P_{Leakage} \quad (14)$$

Then, the 2nd pulse is applied for the measurement of the total polarization ($\hat{P}$) excluding the switching charge density. The 3rd and 4th pulses are used to perform similar tasks but with a negatively biased voltage. Consequently, the gap between $\hat{P}$ and P^* gives the switching charge density (Q_{sw}) as mentioned in eqn (15):

$$Q_{sw} = P^* - \hat{P} \quad (15)$$

Moreover, the derivatives of positive and negative switching polarization can be indicated as P_r^* and $-P_r^*$ and that of positive and negative non-switching polarization can be indicated as $\hat{P}_r$ and $-\hat{P}_r$, respectively.[58]

In this study, all the $Ba_{1-x}Sr_xNiO_3$ samples were analyzed under a 100 V cm^{-1} electric field where pulse width and delay time were kept at 1 ms and 1 s, respectively, for the measurement of the polarization values after each pulse. All the resulting PUND sequences are shown in Fig. 10, where it can be observed that in all the samples, the value of P^* (switching polarization) is greater than that of $\hat{P}$ (non-switching polarization), which corresponds to the contribution of the remanent polarization or the switching charge density. The switching charge density for all the samples was calculated using eqn (15) and plotted against the substitution contents as shown in Fig. 11. It was observed that the Q_{sw} first increases in the intermediate sample BSN-1 and then continuously decreases by increasing the substitution contents. Finally, the lowest value of Q_{sw} was noted in the pure SN sample (Q_{sw} = 2.902 × 10^{-7} μC cm^{-2}) which was quite lower than the value that appeared in the P–E loops. These results clearly state the contribution of the leakage current to the values of the remanent polarizations evaluated by the P–E loops method.

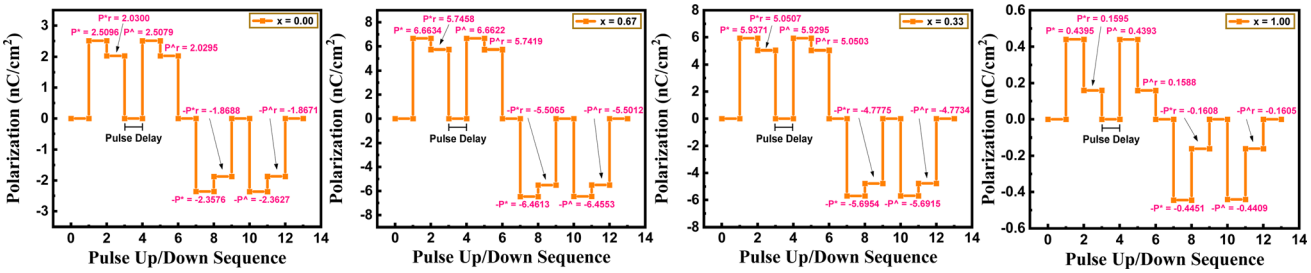

Fig. 10 PUND sequences of the $Ba_{1-x}Sr_xNiO_3$ samples with $x = 0.00$, 0.33, 0.67, and 1.00.

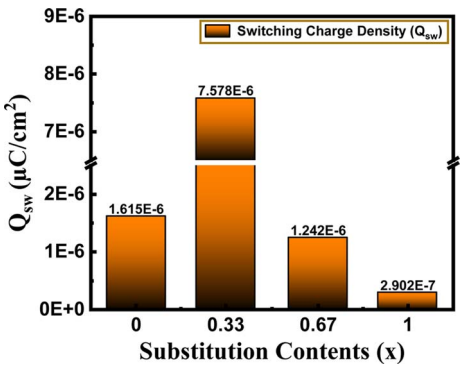

Fig. 11 Switching charge density of the $Ba_{1-x}Sr_xNiO_3$ samples at different substitution contents (x).

4. Conclusion

To conclude, a series of $Ba_{1-x}Sr_xNiO_3$ ($x = 0.00$, 0.33, 0.67, and 1.00) lead-free ceramics was successfully fabricated using the sol–gel auto combustion route. The influence of Sr-substitution on structural, morphological, and ferroelectric responses of ceramics was studied thoroughly. A hexagonal perovskite structure with a $P6_3/mmc$ space group was identified in the XRD spectra of all the samples, which was confirmed using Rietveld's refinement. It was observed that the unit cell volume decreased from 132.06 Å^3 to 120.56 Å^3 and the X-ray density decreased from 6.14 g cm^{-3} to 5.35 g cm^{-3} by increasing the substitution contents. Furthermore, the porosity of the samples was found to be in the range of 22.3% to 34.7%. Using Scherrer's formula and Williamson–Hall plots, the crystallite sizes were calculated and correlated afterwards. The FESEM images revealed that the grain size and agglomeration increased with the increasing Sr-content. In addition, the existence of all the constituent elements according to their stoichiometric ratios was confirmed using the EDX spectra. The ferroelectric analysis showed that by improving the Sr-content, a decrease in the values of the coercive field, maximum polarization, and remanent polarization was obtained, but the recoverable energy density increased as the loops became slimmer. Whereas, the maximum value of recoverable energy density was found in the BSN-2 sample at $x = 0.67$. The minimum energy loss was noted in the pure SN sample with the highest energy storage efficiency (~47.21%). The I–V characteristic curves disclosed the existence of a current barrier up to 1.8×10^{-6} A in all the samples. Moreover, both pure BN and pure SN samples showed a very small conductivity (~10^{-8} Ω^{-1} cm^{-1}). Furthermore, the PUND sequences revealed that the switching charge density decreased with the increasing Sr-content and the lowest was found in the pure SN sample (2.902×10^{-7} μC cm^{-2}). Overall, these findings indicate the potential of this series, especially $SrNiO_3$, in energy storage devices and fast-switching applications. Moreover, the practical applications can also include low powered electronics, spintronics and memory storage devices, *i.e.*, FeRAMs.

Data availability

Data will be made available on request.

Author contributions

Rana Muhammad Ahmad Khan Manj: conceptualization, data curation, formal analysis, writing – original draft. Shahid M. Ramay: software, resources, methodology. M. A. Shar: data curation, formal analysis. Shahzad Naseem: investigation, methodology. Shahid Atiq: methodology, project administration, supervision, writing – review and editing.

Conflicts of interest

The authors declare that they have no known competing financial interests or personal relationships that could have appeared to influence the work reported in this paper.

Acknowledgements

The authors would like to acknowledge the Researchers Supporting Project number (RSP2024R71), King Saud University, Riyadh, Saudi Arabia, for their support of this work.

References

1 Z. Fan, Y. Yu, J. Huang, Q. Zhang, Y. Lu and Y. He, Excellent energy storage properties over a wide temperature range under low driving electric fields in NBT-BSN lead-free relaxor ferroelectric ceramics, *Ceram. Int.*, 2021, **47**, 4715–4721, DOI: 10.1016/j.ceramint.2020.10.040.

2 E. T. Sayed, T. Wilberforce, K. Elsaid, M. K. H. Rabaia, M. A. Abdelkareem, K. J. Chae and A. G. Olabi, A critical review on environmental impacts of renewable energy

systems and mitigation strategies: Wind, hydro, biomass and geothermal, *Sci. Total Environ.*, 2021, **766**, 144505, DOI: 10.1016/j.scitotenv.2020.144505.

3 C. Furlan and C. Mortarino, Forecasting the impact of renewable energies in competition with non-renewable sources, *Renewable Sustainable Energy Rev.*, 2018, **81**, 1879–1886, DOI: 10.1016/j.rser.2017.05.284.

4 H. Qi, A. Xie and R. Zuo, Local structure engineered lead-free ferroic dielectrics for superior energy-storage capacitors: A review, *Energy Storage Mater.*, 2022, **45**, 541–567, DOI: 10.1016/j.ensm.2021.11.043.

5 P. Zhao, Z. Cai, L. Wu, C. Zhu, L. Li and X. Wang, Perspectives and challenges for lead-free energy-storage multilayer ceramic capacitors, *J. Adv. Ceram.*, 2021, **10**, 1153–1193, DOI: 10.1007/s40145-021-0516-8.

6 Z. Yao, Z. Song, H. Hao, Z. Yu, M. Cao, S. Zhang, M. T. Lanagan and H. Liu, Homogeneous/Inhomogeneous-Structured Dielectrics and their Energy-Storage Performances, *Adv. Mater.*, 2017, **29**, 1601727, DOI: 10.1002/adma.201601727.

7 Q. Wang, T. Wang, L. Zhang, Z. Liu, K. Guo, J. Lu and B. Xie, High energy-storage performance of lead-free $Ba_{0.4}Sr_{0.6}TiO_3$–$Sr_{0.7}Bi_{0.2}TiO_3$ relaxor-ferroelectric ceramics with ultrafine grain size, *Ceram. Int.*, 2022, **48**, 2068–2074, DOI: 10.1016/j.ceramint.2021.09.292.

8 Q. Li, K. Han, M. R. Gadinski, G. Zhang and Q. Wang, High Energy and Power Density Capacitors from Solution-Processed Ternary Ferroelectric Polymer Nanocomposites, *Adv. Mater.*, 2014, **26**, 6244–6249, DOI: 10.1002/adma.201402106.

9 K. Zou, Y. Dan, H. Xu, Q. Zhang, Y. Lu, H. Huang and Y. He, Recent advances in lead-free dielectric materials for energy storage, *Mater. Res. Bull.*, 2019, **113**, 190–201, DOI: 10.1016/j.materresbull.2019.02.002.

10 H. Palneedi, M. Peddigari, G. T. Hwang, D. Y. Jeong and J. Ryu, High-Performance Dielectric Ceramic Films for Energy Storage Capacitors: Progress and Outlook, *Adv. Funct. Mater.*, 2018, **28**, 1803665, DOI: 10.1002/adfm.201803665.

11 T. Shao, H. Du, H. Ma, S. Qu, J. Wang, J. Wang, X. Wei and Z. Xu, Potassium-sodium niobate based lead-free ceramics: novel electrical energy storage materials, *J. Mater. Chem. A*, 2017, **5**, 554–563, DOI: 10.1039/c6ta07803f.

12 H. Yang, P. Liu, F. Yan, Y. Lin and T. Wang, A novel lead-free ceramic with layered structure for high energy storage applications, *J. Alloys Compd.*, 2019, **773**, 244–249, DOI: 10.1016/j.jallcom.2018.09.252.

13 B. Luo, X. Wang, E. Tian, H. Song, H. Wang and L. Li, Enhanced energy storage density and high efficiency of lead-free $CaTiO_3$-$BiScO_3$ linear dielectric ceramics, *ACS Appl. Mater. Interfaces*, 2017, **9**, 19963–19972. https://pubs.acs.org/doi/abs/10.1021/acsami.7b04175.

14 T. M. Correia, M. McMillen, M. K. Rokosz, P. M. Weaver, J. M. Gregg, G. Viola and M. G. Cain, A lead-free and high-energy density ceramic for energy storage applications, *J. Am. Ceram. Soc.*, 2013, **96**, 2699–2702, DOI: 10.1111/jace.12508.

15 J. Huang, Z. Fan, S. Gao, Q. Zhang, Y. Lu and Y. He, An effective strategy to realize superior high-temperature energy storage properties in $Na_{0.5}Bi_{0.5}TiO_3$ based lead-free ceramics, *Ceram. Int.*, 2021, **47**, 25794–25799, DOI: 10.1016/j.ceramint.2021.05.307.

16 Y. Zhang, P. Liu, Y. Qin, K. R. Kandula, G. Zhang, Y. Wu, H. Zhang and S. Jiang, Ultrahigh energy storage density of Ca^{2+}-modified PLZST antiferroelectric ceramics prepared by the tape-casting method, *J. Eur. Ceram. Soc.*, 2021, **41**, 4138–4145, DOI: 10.1016/j.jeurceramsoc.2021.02.013.

17 B. Z. Shen, Y. Li and X. Hao, Multifunctional All-Inorganic Flexible Capacitor for Energy Storage and Electrocaloric Refrigeration over a Broad Temperature Range Based on PLZT 9/65/35 Thick Films, *ACS Appl. Mater. Interfaces*, 2019, **11**, 34117–34127, DOI: 10.1021/acsami.9b12353.

18 Y. Yu, Y. Zhang, Y. Zhang, H. Li, Q. Zhang, Y. Lu and Y. He, High-temperature energy storage performances in $(1-x)(Na_{0.50}Bi_{0.50}TiO_3)$-$xBaZrO_3$ lead-free relaxor ceramics, *Ceram. Int.*, 2020, **46**, 28652–28658, DOI: 10.1016/j.ceramint.2020.08.024.

19 S. I. Shkuratov and C. S. Lynch, A review of ferroelectric materials for high power devices, *J. Materiomics.*, 2022, **8**, 739–752, DOI: 10.1016/j.jmat.2022.04.002.

20 L. Zhang, L. X. Pang, W. B. Li and D. Zhou, Extreme high energy storage efficiency in perovskite structured $(1-x)(Ba_{0.8}Sr_{0.2})TiO_3$-$xBi(Zn_{2/3}Nb_{1/3})O_3$ $(0.04 \leq x \leq 0.16)$ ceramics, *J. Eur. Ceram. Soc.*, 2020, **40**, 3343–3347, DOI: 10.1016/j.jeurceramsoc.2020.03.015.

21 Y. Zhang, H. Dan, J. Chen, M. Maraj, W. Wei, B. Peng and W. Sun, Evaluation of energy storage performance of ferroelectric materials by equivalent circuit model, *Ceram. Int.*, 2021, **47**, 20512–20518, DOI: 10.1016/j.ceramint.2021.04.060.

22 K. M. Sangwan, N. Ahlawat, R. S. Kundu, S. Rani, S. Rani, N. Ahlawat and S. Murugavel, Improved dielectric and ferroelectric properties of Mn doped barium zirconium titanate (BZT) ceramics for energy storage applications, *J. Phys. Chem. Solids*, 2018, **117**, 158–166, DOI: 10.1016/j.jpcs.2018.01.051.

23 A. Verma, A. K. Yadav, N. Khatun, S. Kumar, R. Jangir, V. Srihari, V. R. Reddy, S. W. Liu, S. Biring and S. Sen, Structural, dielectric and ferroelectric studies of thermally stable and efficient energy storage ceramic materials: $(Na_{0.5-x}K_xBi_{0.5-x}La_x)TiO_3$, *Ceram. Int.*, 2018, **44**, 20178–20186, DOI: 10.1016/j.ceramint.2018.07.312.

24 G. H. Haertling, Ferroelectric Ceramics: History and Technology, *J. Am. Ceram. Soc.*, 1999, **82**, 797–818, DOI: 10.1111/j.1151-2916.1999.tb01840.x.

25 R. Moussi, A. Bougoffa, A. Trabelsi, E. Dhahri, M. P. F. Graça, M. A. Valente, R. Barille and M. Rguiti, Investigation of the effect of Sr-substitution on the structural, morphological, dielectric, and energy storage properties of $BaTiO_3$-based perovskite ceramics, *Inorg. Chem. Commun.*, 2022, **137**, 109225, DOI: 10.1016/j.inoche.2022.109225.

26 M. Aamir, I. Bibi, S. Ata, K. Jilani, F. Majid, S. Kamal, N. Alwadai, M. A. S. Raza, M. Bashir, S. Iqbal, M. Aadil and M. Iqbal, Ferroelectric, dielectric, magnetic, structural and

photocatalytic properties of Co and Fe doped $LaCrO_3$ perovskite synthesized via micro-emulsion route, *Ceram. Int.*, 2021, **47**, 16696–16707, DOI: 10.1016/j.ceramint.2021.02.240.

27 R. D. King-Smith' and D. Vanderbilt, First-principles investigation of ferroelectricity in perovskite compounds, *Phys. Rev. B: Condens. Matter Mater. Phys.*, 1994, **49**, 5828, DOI: 10.1103/PhysRevB.49.5828.

28 H. Li, F. Li, Z. Shen, S. T. Han, J. Chen, C. Dong, C. Chen, Y. Zhou and M. Wang, Photoferroelectric perovskite solar cells: Principles, advances and insights, *Nano Today*, 2021, **37**, 101062, DOI: 10.1016/j.nantod.2020.101062.

29 N. Ramadass, ABOa-Type Oxides-Their Structure and Properties-A Bird's Eye View, *Mater. Sci. Eng.*, 1978, **36**, 231–239, DOI: 10.1016/0025-5416(78)90076-9.

30 S. Royer, D. Duprez, F. Can, X. Courtois, C. Batiot-Dupeyrat, S. Laassiri and H. Alamdari, Perovskites as substitutes of noble metals for heterogeneous catalysis: Dream or reality, *Chem. Rev.*, 2014, **114**, 10292–10368, DOI: 10.1021/cr500032a.

31 J. Zhang, Y. Lin, L. Wang, Y. Yang, H. Yang and Q. Yuan, Significantly enhanced energy storage density in sodium bismuth titanate-based ferroelectrics under low electric fields, *J. Eur. Ceram. Soc.*, 2020, **40**, 5458–5465, DOI: 10.1016/j.jeurceramsoc.2020.06.059.

32 Y. H. Huang, Y. J. Wu, J. Li, B. Liu and X. M. Chen, Enhanced energy storage properties of barium strontium titanate ceramics prepared by sol-gel method and spark plasma sintering, *J. Alloys Compd.*, 2017, **701**, 439–446, DOI: 10.1016/j.jallcom.2017.01.150.

33 M. S. Khalil and M. A. Wahba, Sr-substitution Effects on La-NiO_3, Sol-Gel Synthesis, Structural and Electrical Properties, *Egypt. J. Chem.*, 2016, **59**, 719–729, DOI: 10.21608/ejchem.2016.1446.

34 M. M. Hasan, A. Kabir and M. Kamruzzaman, The structural, elastic, electronic, magnetic and optical properties of $SrNiO_3$ perovskite: A DFT and DFT+U study, *Results Phys.*, 2022, **41**, 105920, DOI: 10.1016/j.rinp.2022.105920.

35 A. E. Razek Mahmoud and S. K. S. Parashar, Effect of domain switching contribution on polarization current, leakage current and switching charge density studied by PUND method in $(Ba_{1-x},Ca_x)TiO_3$ ceramics, *Mater. Sci. Eng. B*, 2019, **246**, 13–20, DOI: 10.1016/j.mseb.2019.05.022.

36 B. D. Cullity, *Elements of X-Ray Diffraction*, Addison-Wesley Publishing, 1956, pp. 335–336, http://117.239.25.194:7000/jspui/bitstream/123456789/954/1/PRELIMINARY%20AND%20CONTENT.pdf.

37 R. M. García De La Cruz, H. Falcón, M. A. Peña and J. L. G. Fierro, Role of bulk and surface structures of $La_{1-x}Sr_xNiO_3$ perovskite-type oxides in methane combustion, *Appl. Catal., B*, 2001, **33**, 45–55, DOI: 10.1016/S0926-3373(01)00157-6.

38 P. Sharma, P. Kumar, R. S. Kundu, J. K. Juneja, N. Ahlawat and R. Punia, Structural and dielectric properties of substituted barium titanate ceramics for capacitor applications, *Ceram. Int.*, 2015, **41**, 13425–13432, DOI: 10.1016/j.ceramint.2015.07.131.

39 N. Pradhani, P. K. Mahapatra and R. N. P. Choudhary, Structural and impedance analysis of $Bi_{0.5}Na_{0.5}Ti_{0.80}Mn_{0.20}O_3$ ceramics, *Ceram. Int.*, 2020, **46**, 4126–4136, DOI: 10.1016/j.ceramint.2019.10.128.

40 H. J. Choi, J. U. Woo, H. G. Hwang, D. S. Kim, M. Sanghadasa and S. Nahm, Microstructure and dielectric properties of compositionally graded $Ba_{1-x}Sr_xTiO_3$ multilayer tunable capacitors, *J. Eur. Ceram. Soc.*, 2021, **41**, 2559–2567, DOI: 10.1016/j.jeurceramsoc.2020.12.027.

41 A. Quader, G. M. Mustafa, S. Kumail Abbas, H. Ahmad, S. Riaz, S. Naseem and S. Atiq, Efficient energy storage and fast switching capabilities in Nd-substituted $La_2Sn_2O_7$ pyrochlores, *Chem. Eng. J.*, 2020, **396**, 125198, DOI: 10.1016/j.cej.2020.125198.

42 R. Moussi, A. Bougoffa, A. Trabelsi, E. Dhahri, M. P. F. Graça, M. A. Valente and R. Barille, Effect of Sr-substitution on structure, dielectric relaxation and conduction phenomenon of $BaTiO_3$ perovskite material, *J. Mater. Sci.: Mater. Electron.*, 2021, **32**, 11453–11466, DOI: 10.1007/s10854-021-05604-3.

43 M. Kashif, A. Quader, M. A. Khan, S. M. Ramay and S. Atiq, Effectively coupled $BiFeO_3$-$MnFe_2O_4$-Cr_2O_3 tri-phase multiferroic composites for efficient energy storage and fast switching, *J. Alloys Compd.*, 2022, **929**, 167274, DOI: 10.1016/j.jallcom.2022.167274.

44 F. Afzal, M. T. Ansar, A. S. Haidyrah, M. A. Khan, G. M. Mustsfa, M. Saleem and S. Atiq, A neoteric tri-phase composite with efficient magneto-electric and multifunctional response, *J. Alloys Compd.*, 2021, **888**, 161516, DOI: 10.1016/j.jallcom.2021.161516.

45 Y. Pu, L. Zhang, Y. Cui and M. Chen, High Energy Storage Density and Optical Transparency of Microwave Sintered Homogeneous $(Na_{0.5}Bi_{0.5})(1\text{-}x)Ba_xTi(1\text{-}y)Sn_yO_3$ Ceramics, *ACS Sustain. Chem. Eng.*, 2018, **6**, 6102–6109, DOI: 10.1021/acssuschemeng.7b04754.

46 J. Junita, D. Jayalakshmi and J. D. Rodney, Effect of annealing temperature on the bifunctional electrocatalytic properties of strontium nickelate ($SrNiO_3$) nanoparticles for efficient overall water splitting, *Int. J. Hydrog. Energy*, 2022, **47**, 30602–30612, DOI: 10.1016/j.ijhydene.2022.07.007.

47 M. Zahid, M. Younis, T. A. Khan, M. Ahmad, A. Quader, G. M. Mustafa, E. A. Alghamdi, S. M. Ramay, H. Chang and S. Atiq, Strain induced electromagnetic coupling in tri-phase multiferroic composites $0.8[(1\text{-}x)Fe_2O_3$–$xPbZrO_3]$+$0.2Cr_2O_3$ for multistate devices, *Ceram. Int.*, 2022, **48**, 27560–27567, DOI: 10.1016/j.ceramint.2022.06.049.

48 M. Umair, A. Quader, M. Imran, M. A. Yaqub, S. M. Ramay and S. Atiq, Significant impact of spinel ferrites in evolution of magneto-electric coupling in novel tri-phase composites, *Ceram. Int.*, 2022, **48**, 14473–14480, DOI: 10.1016/j.ceramint.2022.01.340.

49 M. I. Khan and T. C. Upadhyay, General Introduction to Ferroelectrics, Multifunctional Ferroelectric Materials, *Intechopen*, 2021, 7–29, DOI: 10.5772/intechopen.92527.

50 M. Manikandan, K. Saravana Kumar and C. Venkateswaran, Mn doping instigated multiferroicity and magneto-dielectric

coupling in $KNbO_3$, *J. Appl. Phys.*, 2015, **118**, 234105, DOI: 10.1063/1.4938118.

51 H. Yang, F. Yan, Y. Lin and T. Wang, Enhanced recoverable energy storage density and high efficiency of $SrTiO_3$-based lead-free ceramics, *Appl. Phys. Lett.*, 2017, **111**, 253903, DOI: 10.1063/1.5000980.

52 H. L. Schwartz, T. M. Miller and B. Bederson, Measurement of the static electric dipole polarizabilities of barium and strontium, *Phys. Rev. A: At., Mol., Opt. Phys.*, 1924, **10**, 1974, DOI: 10.1103/PhysRevA.10.1924.

53 D. Zhang, W. Liu, R. Guo, K. Zhou and H. Luo, High Discharge Energy Density at Low Electric Field Using an Aligned Titanium Dioxide/Lead Zirconate Titanate Nanowire Array, *Advanced Science*, 2018, **5**, 1700512, DOI: 10.1002/advs.201700512.

54 F. Akram, M. Sheeraz, A. Hussain, I. W. Kim, T. H. Kim and C. W. Ahn, Thermally-stable high energy-storage performance over a wide temperature range in relaxor-ferroelectric $Bi_{1/2}Na_{1/2}TiO_3$-based ceramics, *Ceram. Int.*, 2021, **47**, 23488–23496, DOI: 10.1016/j.ceramint.2021.05.065.

55 M. A. Yaqub, S. Niaz, S. Khan, A. Quader, S. M. Ramay, S. K. Abbas and S. Atiq, Ternary composites: A suitable platform for simultaneous improvement of multiferroic characteristics, *Mater. Sci. Semicond. Process.*, 2022, **147**, 106728, DOI: 10.1016/j.mssp.2022.106728.

56 A. Sigov, Y. Podgorny, K. Vorotilov and A. Vishnevskiy, Leakage currents in ferroelectric thin films, *Phase Transitions*, 2013, **86**, 1141–1151, DOI: 10.1080/01411594.2013.790033.

57 J. F. Scott, C. A. Araujo, H. B. Meadows, L. D. McMillan and A. Shawabkeh, Radiation effects on ferroelectric thin-film memories: Retention failure mechanisms, *J. Appl. Phys.*, 1989, **66**, 1444–1453, DOI: 10.1063/1.344419.

58 A. E. Razek Mahmoud, M. Ezzeldien and S. K. S. Parashar, Enhancement of switching/un-switching leakage current and ferroelectric properties appraised by PUND method of $(Ba_{1-x}Ca_x)TiO_3$ lead free piezoelectric near MPB, *Solid State Sci.*, 2019, **93**, 44–54, DOI: 10.1016/j.solidstatesciences.2019.04.011.